SUPPLEMENTAL MATERIALS

ASCE *Journal of Geotechnical and Geoenvironmental Engineering*

Experimental Study of the Earth Pressure Evolution on a Model Wall Rotating about Its Base

David Perozzi and Alexander M. Puzrin

DOI: 10.1061/JGGEFK.GTENG-12163

www.ascelibrary.org

MECHANICAL SYSTEM OF THE MODEL WALL AND CALIBRATION OF ITS ROTATIONAL STIFFNESS

The simplified mechanical system of a wall section is sketched in Fig. S1a. The system consists of a simply supported L-shaped beam, representing the wall stem and the cantilever plate connected to it, and the lower cantilever plate connected to the base plate of the wall. These two parts are connected by the structure that supports the linear actuator and the load cell. This structure contains two hinges and can, therefore, be represented as a bar with stiffness EA_4. The wall stem is assumed to have an approximately constant bending stiffness EI_1, whereas the two cantilever plates clearly have a variable bending stiffness along their length. As the base plate of the wall rests on a rigid surface, the cantilever plate connected to it can be assumed to be clamped.

When a load $q(y)$ is applied, the wall stem undergoes a deflection and a rigid body rotation, as shown in Fig. S1b. Here, $q(y)$ is drawn as linearly distributed, although its distribution is arbitrary and does not affect the rest of this section. The rigid body rotation is due to the deformation of beams 2 and 3, and that of bar 4. In the case of real retaining walls, a rigid body rotation of the wall stem about its base usually occurs because of the presence of a lap splice right above the construction joint (see Haefliger and Kaufmann 2023).

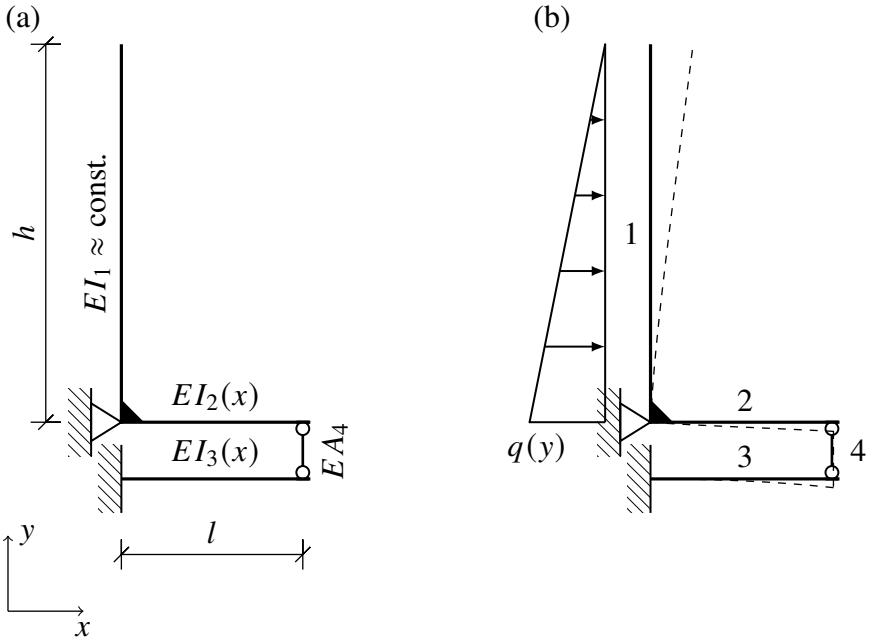

Fig. S1. Simplified mechanical system of a wall section. (a): Properties; (b) Forces and deformations (qualitative).

For the model walls, the individual quantification of the deflection of beams 2 and 3, and the compression of bar 4 is not of interest. The only value of interest is the rigid body rotation of the stem. Therefore, the mechanical system shown in Fig. S1a can be further simplified. The simplification steps are illustrated in Fig. S2. First, the lower cantilever plate and the bar connecting it to the upper plate can be replaced by a linear spring (Fig. S2b). Then, the system can be further

simplified by replacing the upper cantilever plate and the linear spring with a rotational spring characterized by the stiffness c_f, as in Fig. S2c.

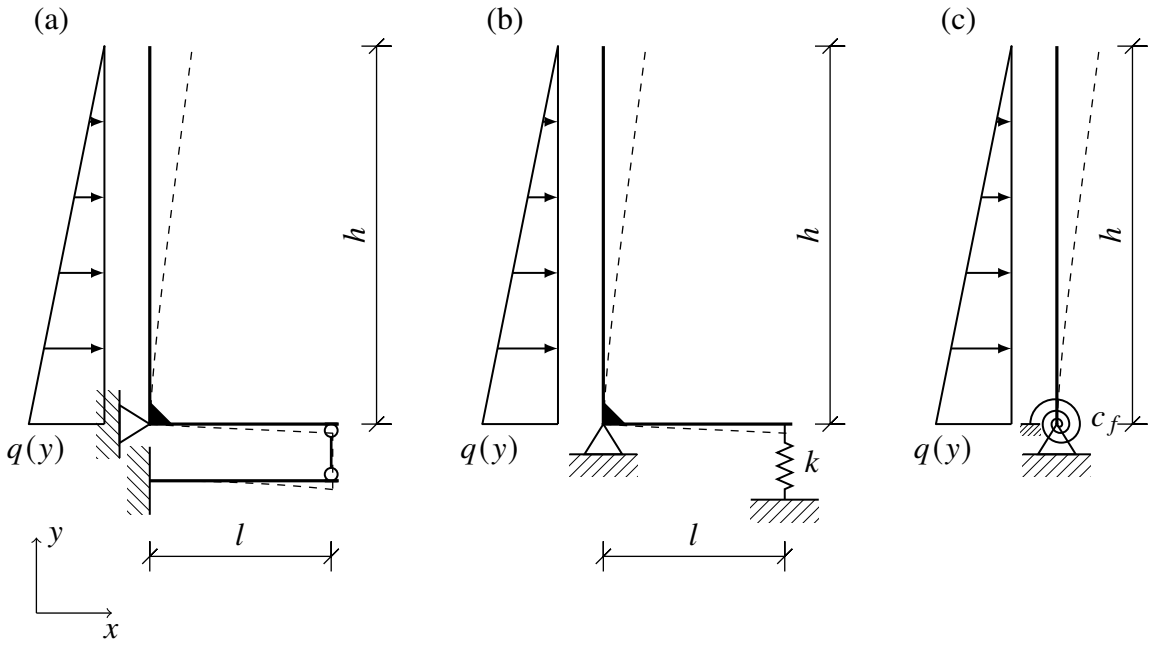

Fig. S2. Statically equivalent system of the mechanical system of a wall section.

The knowledge of the stiffness c_f is necessary for the cross-validation of the wall rotation measurement against the position of the linear actuator and for a possible numerical simulation of the experiments. Its value was determined in a test that consisted of applying a line load at the top of the wall (which generated a bending moment m at the wall base) and measuring the rotation of the axis θ (see Fig. S3). Using the linear least squares method, the values in Table S1 were obtained.

TABLE S1. Rotational stiffness and Young's modulus of the stem for each wall section.

Property	Unit	Wall A	Wall B	Wall C
Rotational stiffness c_f	(N/mrad)	140	123	165
Young's modulus E	(MPa)	3245	3437	3410

VALIDATION OF THE STRAIN MEASUREMENTS

Similar to the methods used in the previous section, the strain measurements were validated by applying a known line load at the top of the wall. The resulting strain distribution over the wall height, shown in Fig. S4, was compared with the expected strain distribution assuming the wall behaves as an Euler-Bernoulli beam. These measurements allowed the Young's modulus of

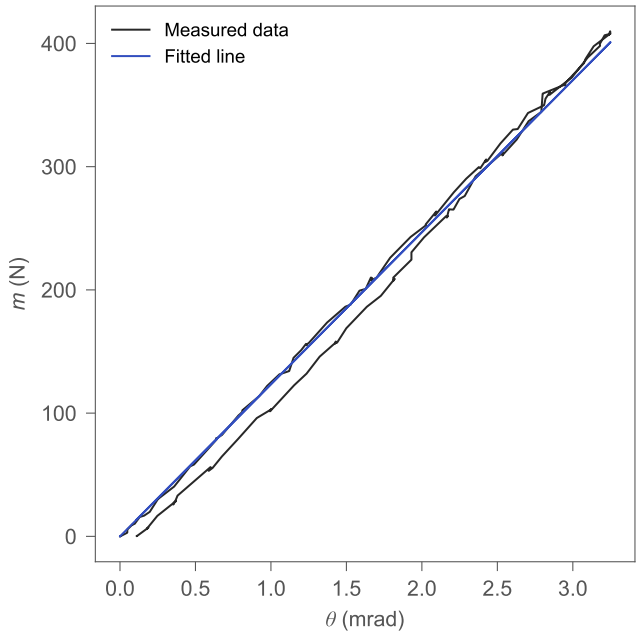

Fig. S3. Calibration of the rotational stiffness of a wall section (wall B).

unplasticized polyvinyl chloride (uPVC) to be determined by linear least squares analysis. The Young's modulus values obtained are summarized in Table S1 and show excellent agreement with the expected value of 3500 MPa as given in uPVC data sheets. This correlation underscores the validity of the strain measurement methodology and material property assumptions used in this study.

CROSS-VALIDATION OF STRESS AND MOMENT MEASUREMENTS

An advantage of the developed experimental setup is the redundancy of the measurements, which allows cross-validation of each measurement with an independent one. For example, stress measurements can be integrated to estimate the moment acting on the wall hinge. This integrated moment is shown in Fig. S5. A good agreement is observed between the integrated and direct measurements of the moment, both showing the same qualitative trend, with only a small deviation between them.

Clearly, the direct measurement based on the force transmitted by the linear actuator to the base plate is more accurate, as it directly measures the integrated quantity. In contrast, the stress measurements have a lower spatial resolution (i.e. only eight measurements over the wall height — linearly interpolated between them), have to be extrapolated close to the wall base, and are more susceptible to noise (given the small magnitudes of the measured quantities). In particular, the integration of stresses measured in dense soil tests seems less accurate. The main reason is that a stress increase was observed near the bottom of the wall. Based on the two lowest measurements, the stress distribution is linearly extrapolated, leading to overestimating the stress near the base.

The presented results confirm the accuracy of the designed measuring system. Of course, each device has its own purpose. The pressure transducers proved to be excellent for determining the stress acting on the wall at different points and its distribution. However, the reduced spatial

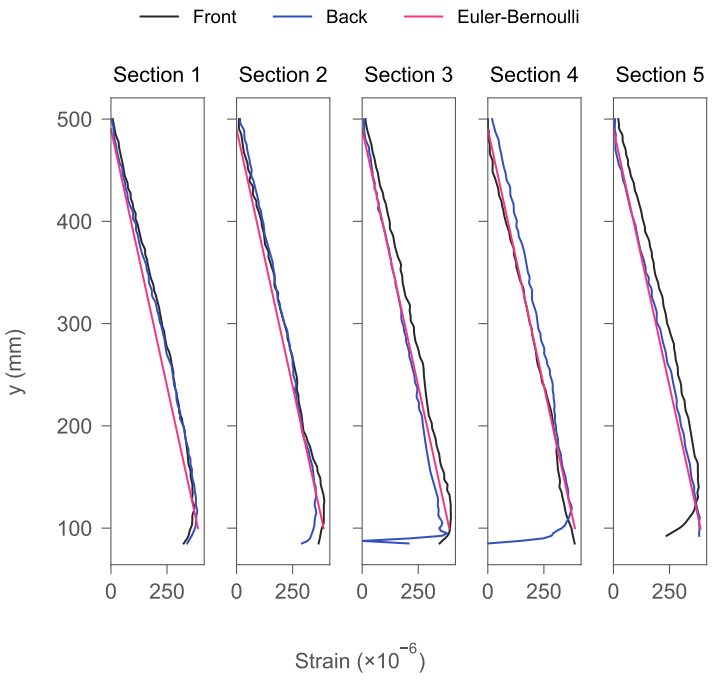

Fig. S4. Test of the fiber optic measurement system (wall B). *Front* indicates the fibers on the front side of the wall, *Back* those on the side of the backfill.

resolution makes them less suitable for determining the total load acting on the wall. For this purpose, an external force transducer was used.

WALL DEFLECTION AND EARTH PRESSURE DISTRIBUTIONS

The earth pressure distribution and the wall deflection measured at the end of the backfill phase are shown in Figs. S6 and S7.

The earth pressure distribution measured at the end of the rotation phase is shown in Fig. S8.

ROTATION-DEPENDENT EVOLUTION OF THE MOMENT ON ALL WALL SECTIONS DURING A PLANE-STRAIN TEST

Fig. S9 shows the different moment-rotation responses for each wall section in the case of dense and loose backfill. The moment acting on Wall B, the central section, was higher than on the lateral sections A and C. This discrepancy, caused by boundary effects such as friction between the glass wall and the soil, was anticipated and taken into account in the design of the wall (i.e., it led to the design of independent sections). Differences in initial conditions, such as slight variations in backfill height or friction between the rotating wall and the box, explain the divergent measurements of walls A and C in test C2D (Fig. S9b).

FAILURE MECHANISM

Figs. S10 and S11 show a side view of the failure mechanisms in dense and loose sand tests. This side-viewed deformation only offers *qualitative insight*, as boundary effects influence the soil deformation. Despite being curved, the failure mechanism can be reasonably approximated by a straight line.

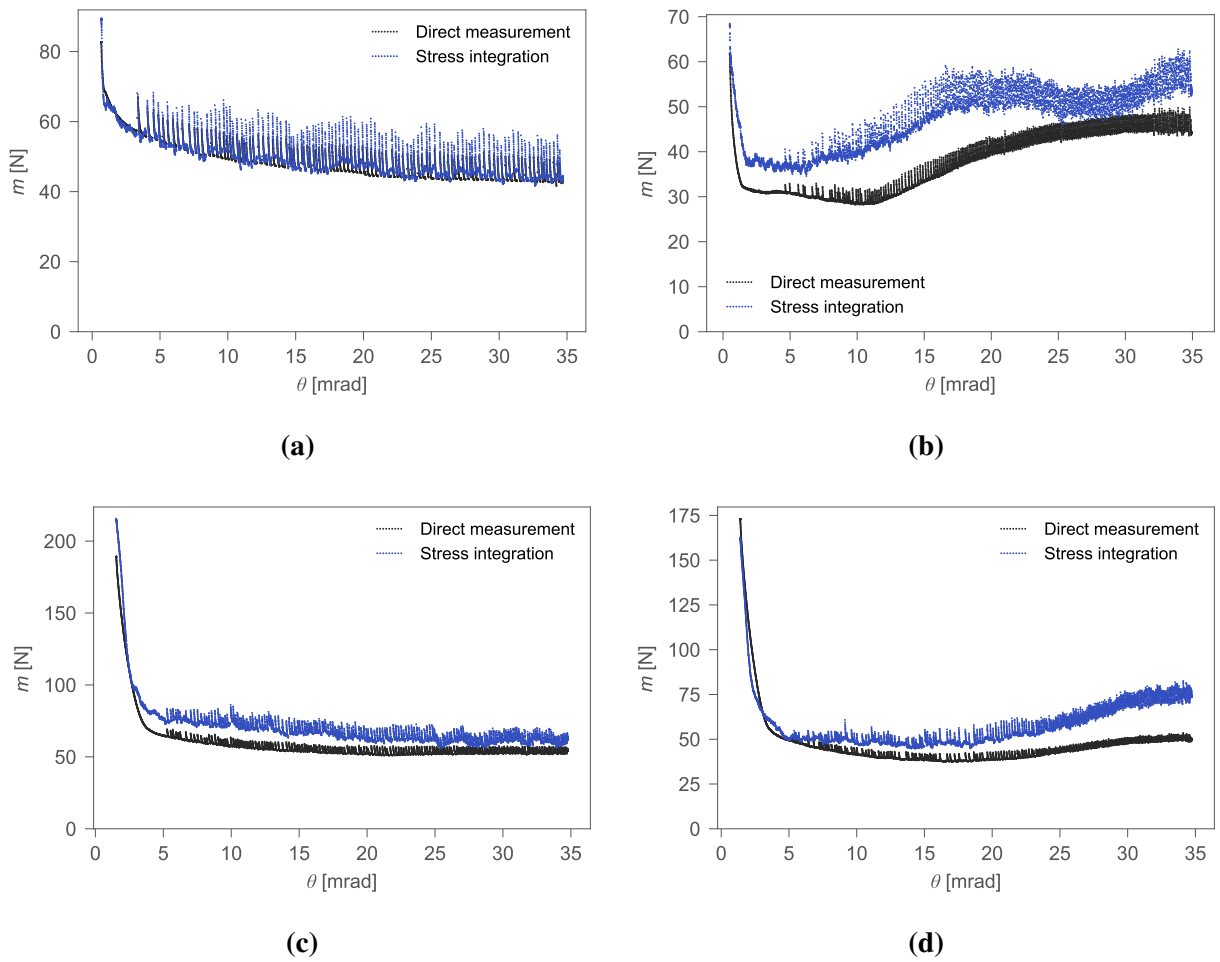

Fig. S5. Comparison of the moment determined from the direct measurement of the force acting on the linear actuator and from the integration of the lateral earth pressure measured by the pressure sensors. (a) Test C3L; (b) Test C4D; (c) Test C5Lc; (d) Test C6Dc.

COMPARISON OF 2D VS 3D TESTS

Fig. S12 compares the normalized bending moment acting at the wall base for tests carried out under three-dimensional and plane strain conditions with soil having the same relative density.

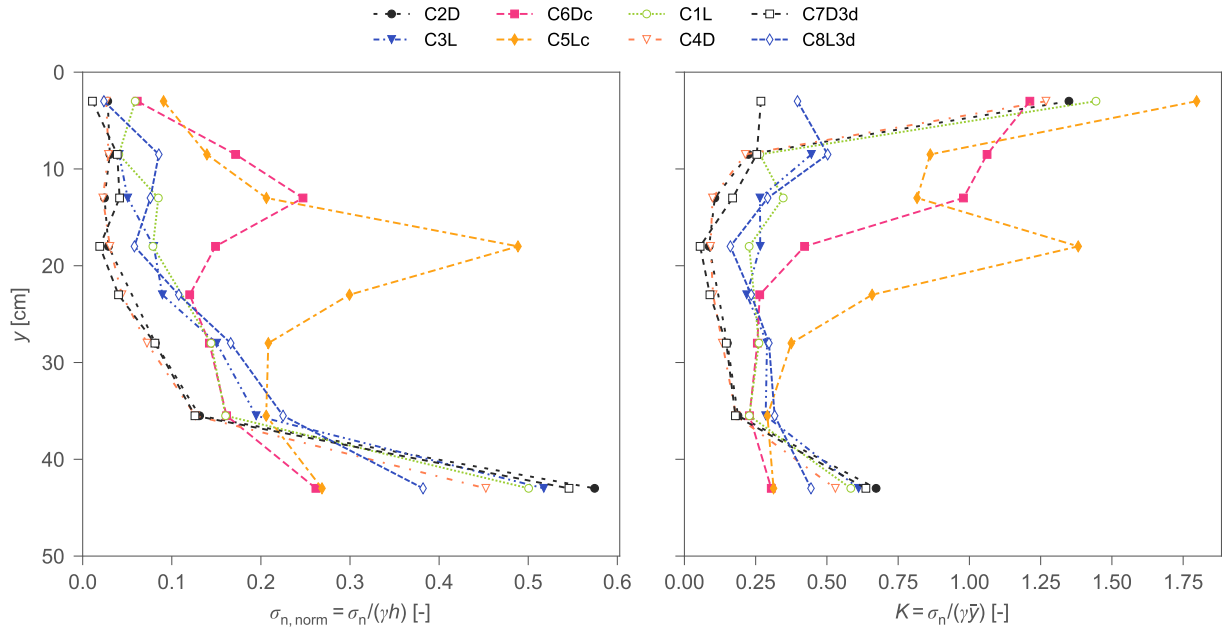

Fig. S6. Earth pressure distribution measured at the end of the backfill phase.

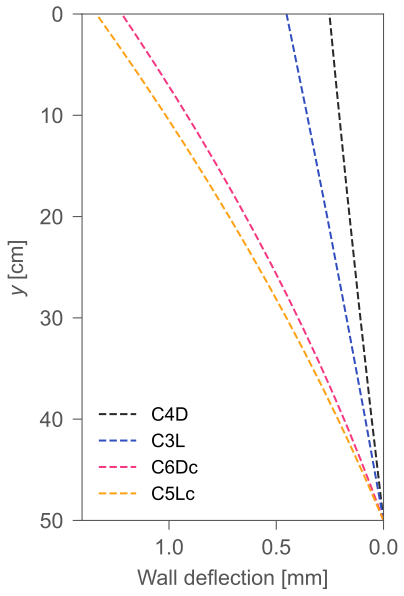

Fig. S7. Wall deflection measured at the end of the backfill phase.

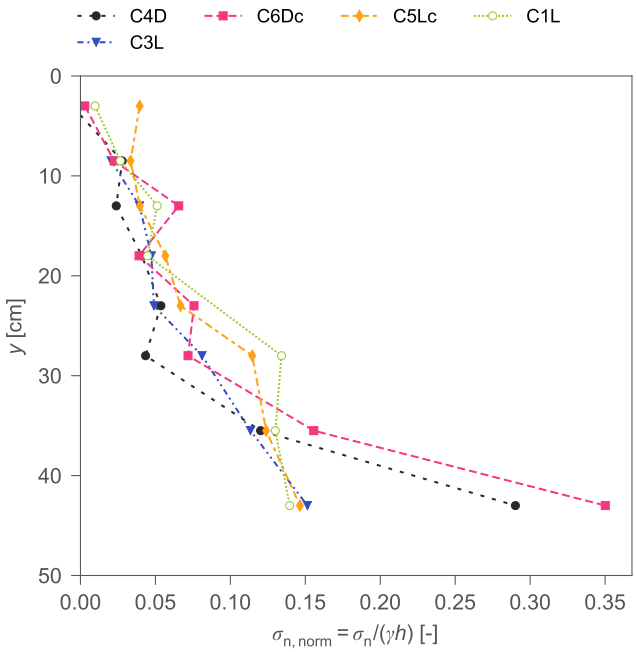

Fig. S8. Earth pressure distribution measured at the end of the rotation phase.

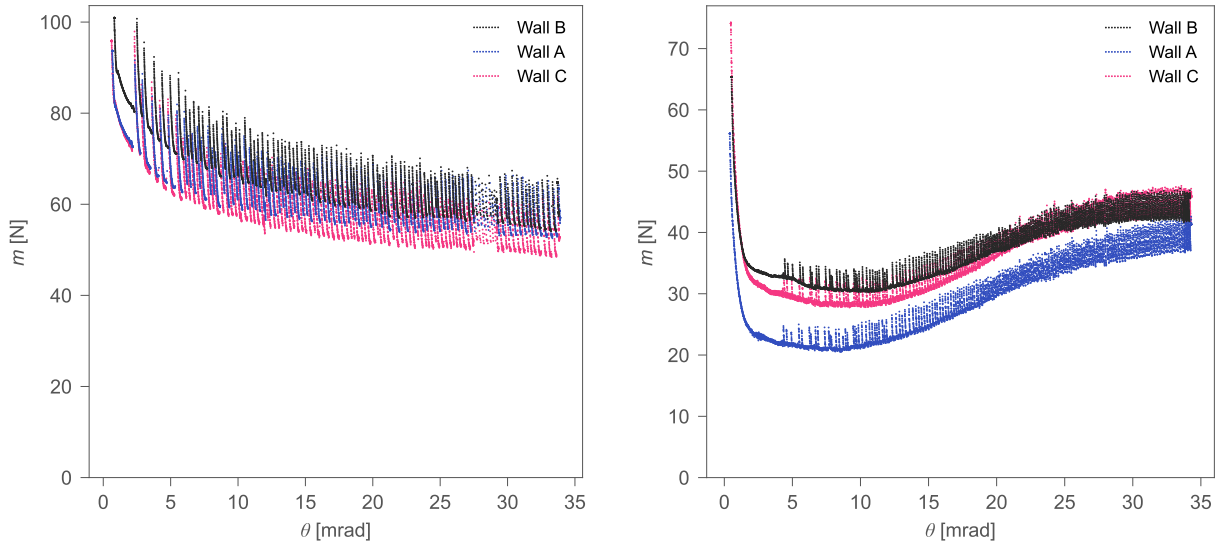

Fig. S9. Moment versus wall rotation measured on all wall sections at the base of the stem during the rotation phase in (a) Test C1L; (b) Test C2D.

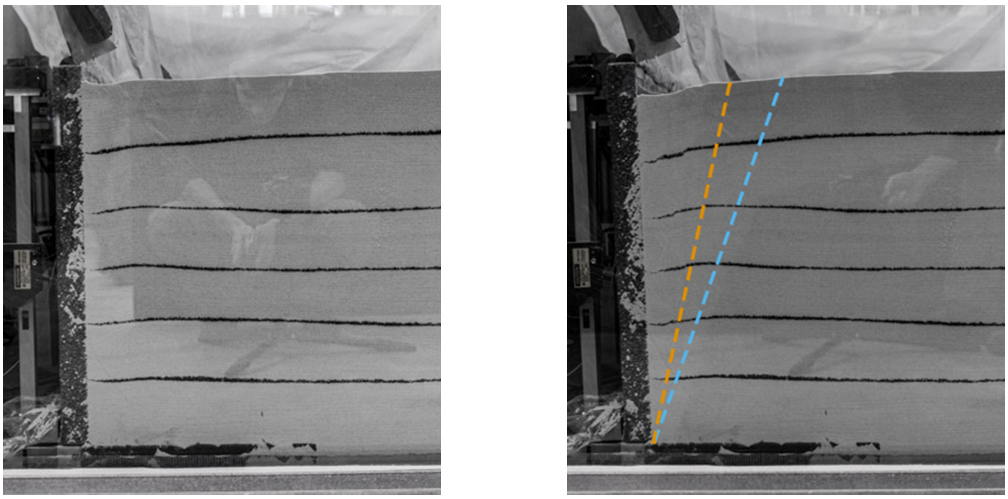

(a) **(b)**

Fig. S10. Side view of the backfill at the beginning (a) and at the end (b) of the rotation phase in test C6Dc. The orange line marks approximately the rightmost strongly localized slip line, and the blue line delimits the region where deformation occurs.

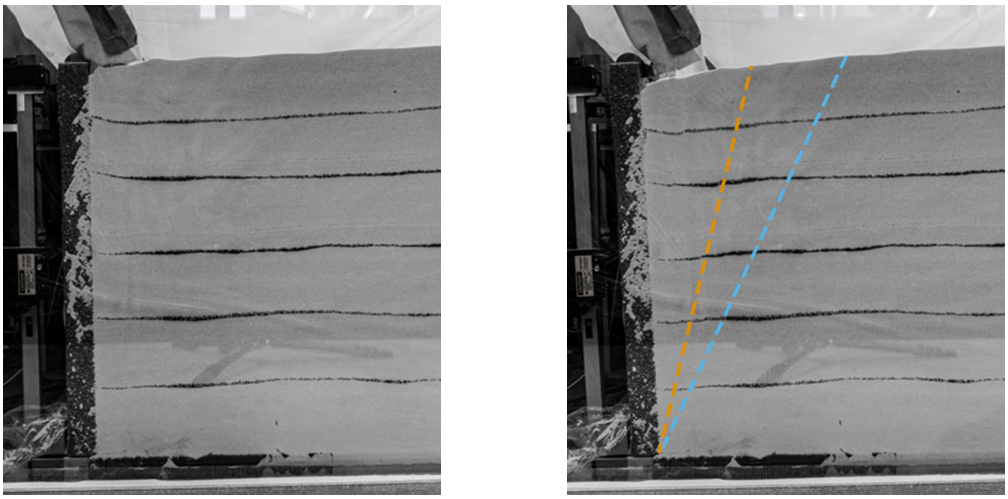

(a) **(b)**

Fig. S11. Side view of the backfill at the beginning (a) and at the end (b) of the rotation phase in test C5Lc. The orange line marks approximately the rightmost strongly localized slip line, and the blue line delimits the region where deformation occurs.

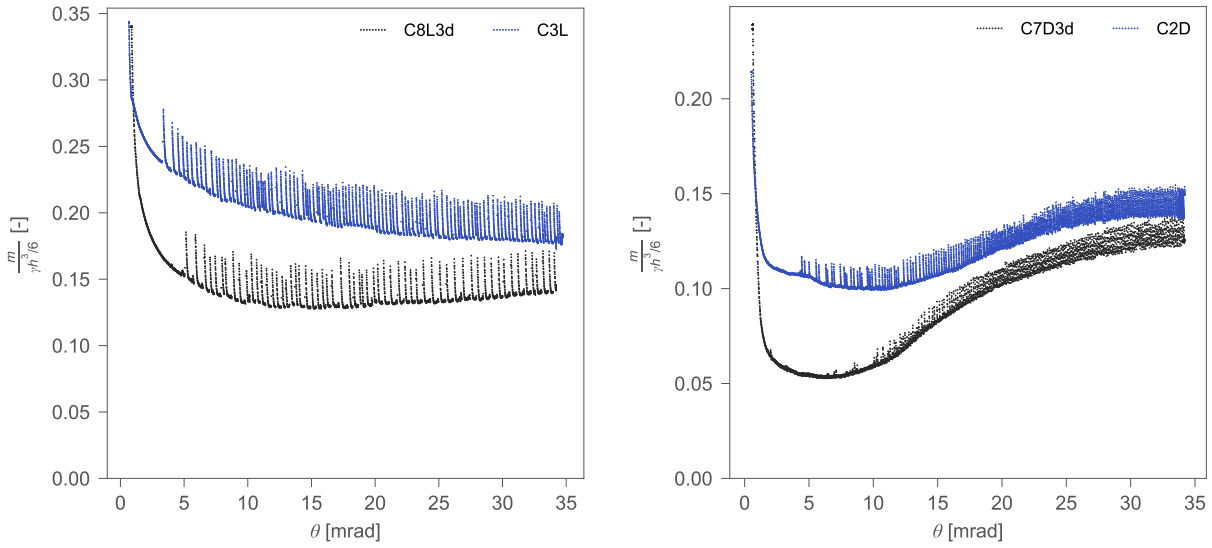

(a) **(b)**

Fig. S12. Comparison of the moment on the central section as a function of its rotation for the tests carried out under 2D (blue) and 3D (black) conditions and using (a) loose sand; (b) dense sand.

REFERENCES

Haefliger, S. and Kaufmann, W. (2023). "Load-deformation behavior of locally corroded reinforced concrete retaining wall segments: Experimental results." *Structural Concrete*, 24(1), 288–317 doi: 10.1002/suco.202200405.